Simulation of a reactive fluidized bed reactor using CFD/DEM

Yann Dufresne, Vincent Moureau, Enrica Masi, Olivier Simonin, Jeremy Horwitz

Simulation of a reactive fluidized bed reactor using CFD/DEM

By Y. Dufresne†, V. Moureau†, E. Masi, O. Simonin‡ AND J. Horwitz

This report presents the numerical study of a semi-industrial fluidized bed, which involves a reactive fluid phase and an inert granular phase. The simulations are based on a meso-scale approach using the Discrete Element Method (DEM) to represent the Lagrangian phase behavior coupled with Large-Eddy Simulation (LES) for the fluid phase. To cope with the limiting ratio between mesh and particle size stemming from the CFD/DEM modeling, a dynamic thickened flame approach is used. This approach yields interesting results regarding the prediction of the bed critical temperature.

1. Introduction

Fluidized-bed reactors (FBR) are found in a large variety of industrial processes ranging from coal gasification to water treatment. In such devices, the fluidization regime occurs when the fluid that passes through the granular material exceeds the minimum fluidization velocity. In this regime, the drag force applied to the solid grains counterbalances gravity, which leads to a strong mixing of the fluid and solid phases. This mixing ensures efficient heat, and mass transfers across the reactor and minimizes temperature and species concentration gradients in the fluidized region. These properties are particularly interesting in reactive FBR to achieve low-temperature combustion with high conversion efficiency and low pollutant emissions such as nitrogen oxides.

Numerical simulation of FBR is very challenging to impart because of the multi-scale nature of the flow. The ratio of the reactor size to the solid particle diameter is very large. While momentum, heat and mass transfers occur at the particle scale, the fluidization regime may feature large void regions or "bubbles" with bursting dynamics that need to be captured. In reactive FBR, chemical reactions occur both in the dense and in the void regions. The solid particles have dual effects on the reactions: i) they heat up and mix the fresh gases and ii) they quench the reactions when gas temperature exceeds the solid temperature. Understanding and optimization of such devices require a very detailed modeling of these competing effects.

The objective of this paper is to gain insight into FBR dynamics using high-fidelity simulations based on a coupled CFD/DEM approach. The chosen configuration is a semi-industrial FBR filled with sand beads and fed with a mixture of natural gas and air, which is operated in the bubbling regime (Dounit *et al.* 2001, 2008). This configuration, which is illustrated in Figure 1, features an air cooling system, which enables it to have a constant bed temperature. The bed height inside the FBR is approximately 40 cm. Measurements presented in Figure 1 show that above a critical temperature of 800°C, no temperature increase is observed in the freeboard region, i.e., all reactions occur in the dense region

† INSA de Rouen / CORIA, France
‡ Institut de Mécanique des Fluides de Toulouse (IMFT), France

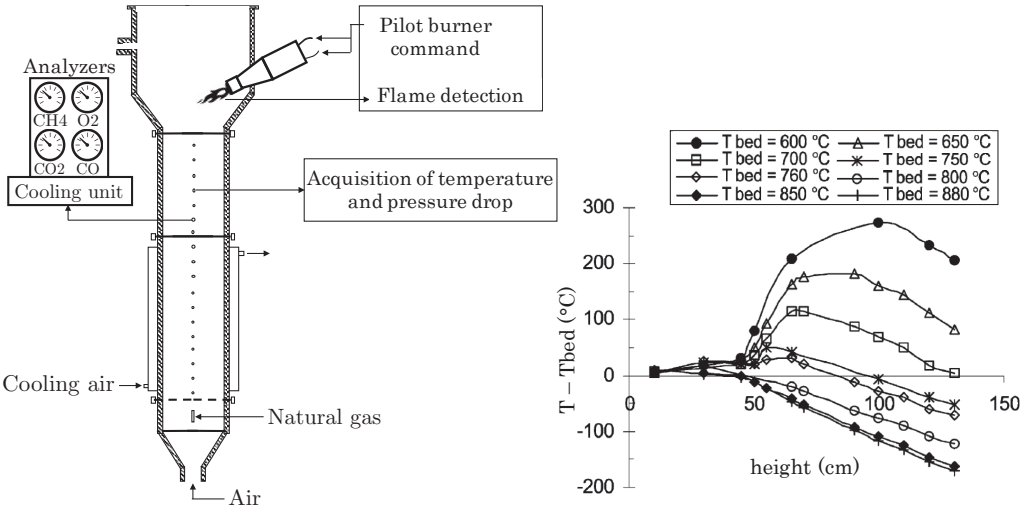

Figure 1: Fluidized bed reactor experimental configuration from Dounit *et al.* (2008).

of the reactor. Below this critical temperature, part of the reactions take place in the freeboard region, leading to an increase in the relative temperature.

The critical temperature results from a complex interplay of mixing, combustion, and heat exchanges between the two phases. Since the bed temperature is constant, a first modeling approach consists of considering the sand particle temperature constant. Then the choice of the combustion and heat transfer models becomes crucial to get the correct critical FBR temperature. The aim of this paper is twofold: to evaluate different combustion models in well-controlled cases of increasing complexity and to apply the modeling approach to the semi-industrial FBR of Figure 1.

Since the full DNS at the particle scale of such FBR configuration is intractable with current computing platforms, a mesoscopic-scale approach based on DEM and LES is chosen. In this four-way-coupled approach, the Eulerian grid size for the fluid is a few times larger than the diameter of the particles, which requires a proper sub-filter modeling of the momentum and heat transfers at the particle surface. These sub-filter models need to take into account the presence of neighboring particles when the local solid volume fraction is important. Such a modeling approach has been successfully applied to the study of particle-laden turbulent flows (Esteghamatian *et al.* 2015; Capecelatro & Desjardins 2013). It allows us to capture and analyze a significant part of the hydrodynamic, thermal, and chemical coupling dynamics, which play a determinant role in the performance of FBRs.

The Euler-Euler formalism featuring two fluid phases has been previously used by

Hamidouche *et al.* (2015, 2016) to study this configuration. Despite good agreement with the experimental data regarding the methane fraction along the bed, results have shown that a mesh refinement could lead to an inaccurate prediction of the maximum gas temperature location, thus decreasing the precision on the species profiles. These difficulties might be overcome using CFD/DEM, as it requires lesser submodeling effort.

2. Modeling approach

2.1. *DEM/LES governing equations*

2.1.1. *Gas phase*

The LES governing equations for the gaseous phase are obtained from the filtering of the unsteady, low-Mach number, Navier-Stokes equations (Capecelatro & Desjardins 2013). If G is the filtering kernel with a characteristic length δ_f, the local fluid fraction is defined as $\varepsilon(\mathbf{x},t) = \int_{V_f} G(|\mathbf{x}-\mathbf{y}|)d\mathbf{y}$, where V_f is the volume occupied by the fluid. Defining $a(\mathbf{x},t)$ as any point property of the fluid, the volume filtered field $\bar{a}(\mathbf{x},t)$ refers to the regular spatial average and is computed by taking the convolution product with the filtering kernel G, giving $\varepsilon\bar{a}(\mathbf{x},t) = \int_{V_f} a(\mathbf{y},t)G(|\mathbf{x}-\mathbf{y}|)d\mathbf{y}$. The term $\tilde{a}(\mathbf{x},t)$ refers to the density-weighted Favre average, written as $\tilde{a}(\mathbf{x},t) = \overline{\varepsilon\rho(\mathbf{x},t)a(\mathbf{x},t)}/\overline{\varepsilon\rho(\mathbf{x},t)}$. Then, the governing equations read

$$\frac{\partial}{\partial t}\left(\varepsilon\bar{\rho}\right) + \nabla.\left(\varepsilon\bar{\rho}\tilde{\mathbf{u}}\right) = 0, \tag{2.1}$$

$$\frac{\partial}{\partial t}\left(\varepsilon\bar{\rho}\tilde{\mathbf{u}}\right) + \nabla.\left(\varepsilon\bar{\rho}\tilde{\mathbf{u}}\otimes\tilde{\mathbf{u}}\right) = -\nabla\bar{P} + \nabla.\left(\varepsilon\bar{\tau}\right) + \varepsilon\bar{\rho}\mathbf{g} + \mathbf{F}_{p\to f}, \tag{2.2}$$

$$\frac{\partial}{\partial t}\left(\varepsilon\bar{\rho}\tilde{h_s}\right) + \nabla.\left(\varepsilon\bar{\rho}\tilde{\mathbf{u}}\tilde{h_s}\right) = \frac{D\bar{P}}{Dt} + \nabla.\left(\varepsilon(\lambda+\lambda_t)\nabla\tilde{T}\right) + \bar{\dot{Q}}_{p\to f} + \bar{\dot{\omega}}_T. \tag{2.3}$$

These equations are supplemented by the ideal gas equation of state. $\mathbf{u}$, ρ, h_s, T, and P are respectively the velocity, density, sensible enthalpy, temperature, and pressure. λ_t is the turbulent thermal diffusivity, defined as the ratio of the turbulent viscosity and a constant turbulent Prandtl number $\lambda_t = \mu_t/Pr_t$. The term $\bar{\dot{\omega}}_T$ is the thermal source term due to combustion reaction exothermicity.

2.1.2. *Solid phase*

Particle movement is given by Newton's second law

$$m_p\frac{d\mathbf{u}_p}{dt} = \mathbf{F}_D + \mathbf{F}_G + \mathbf{F}_C \quad \text{and} \quad \frac{d\mathbf{x}_p}{dt} = \mathbf{u}_p, \tag{2.4}$$

where m_p, $\mathbf{u}_p$, and $\mathbf{x}_p$ are the particle mass, velocity, and position, $\mathbf{F}_D$ is the drag force, $\mathbf{F}_G$ is the gravity force, and $\mathbf{F}_C$ is the collision force.
The total collision force $\mathbf{F}_C$ acting on particle a is computed as the sum of all forces $\mathbf{f}^{col}_{b\to a}$ exerted by the N_p particles and N_w walls in contact. As particles and walls are treated similarly during collisions, the b index refers to both. The soft sphere model from Cundall & Strack (1979) is used along with a damped linear spring and a simple Coulomb sliding model respectively accounting for the normal ($\mathbf{f}^{col}_{n,b\to a}$) and tangential ($\mathbf{f}^{col}_{t,b\to a}$) contact forces. For one particle (or wall) b acting on a particle a,

$$\begin{array}{l|l} \mathbf{F}_C = \sum_{b=1}^{N_p+N_w}\mathbf{f}^{col}_{b\to a} & \mathbf{f}^{col}_{n,b\to a} = \begin{cases} -k_n\delta_{ab}\mathbf{n}_{ab} - 2\gamma_n M_{ab}\mathbf{u}_{ab,n} & \text{if } \delta_{ab}>0, \\ 0 & \text{else.} \end{cases} \\ \mathbf{f}^{col}_{b\to a} = \mathbf{f}^{col}_{n,b\to a} + \mathbf{f}^{col}_{t,b\to a} & \mathbf{f}^{col}_{t,b\to a} = -\mu_{tan}\|\mathbf{f}^{col}_{n,b\to a}\|\mathbf{t}_{ab} \end{array} \tag{2.5}$$

This model requires three user-defined parameters; k_n, γ_n, and μ_{tan} respectively account for the spring stiffness, damping, and friction coefficient of the $a-b$ binary system. The term δ_{ab} is defined as the overlap between the a and b entities, and $M_{ab} = (1/M_a + 1/M_b)^{-1}$ as the system effective mass.

The drag force $\mathbf{F}_D$ acting on a particle p is written

$$\mathbf{F}_D = \frac{\pi}{8} d_p \mu_f C_D \mathrm{Re}_p (\tilde{\mathbf{u}} - \mathbf{u}_p) \quad \text{with} \quad \mathrm{Re_p} = \frac{\varepsilon ||\tilde{\mathbf{u}} - \mathbf{u}_\mathrm{p}|| \mathrm{d_p}}{\nu_\mathrm{f}}\,, \tag{2.6}$$

where d_p is the particle diameter, ν_f and μ_f are the gas kinematic and dynamic viscosities, and C_D is the drag coefficient. In order to compute C_D, Ergun (1952) and Wen & Yu (1966) closures are used.

$$C_D = \begin{cases} C_{D,WY} = \begin{cases} \dfrac{24}{\mathrm{Re}_p}\left(1 + 0.15\mathrm{Re}_p^{0.687}\right)\varepsilon^{-3.7} & \text{for } \mathrm{Re}_p < 10^3 \\ 0.44\varepsilon^{-3.7} & \text{for } \mathrm{Re}_p \geq 10^3 \end{cases} & \text{if } \varepsilon \geq 0.8, \\ C_{D,ER} = \left(200\dfrac{1-\varepsilon}{\mathrm{Re}_p} + \dfrac{7}{3}\right)\varepsilon^{-2} & \text{if } \varepsilon < 0.8. \end{cases} \tag{2.7}$$

The coupling term in Navier-Stokes Eq. (2.2) is written in order to ensure momentum conservation:

$$\mathbf{F}_{p\to f} = -\frac{1}{\Delta V}\sum^{Np} \mathbf{F}_D\,. \tag{2.8}$$

2.2. *Heat transfer from the solid to the gas phase*

Time advancement of the particle temperature caused by heat transfer from the fluid phase is solved, necessitating a closure to estimate the heat transfer coefficient h depending on the Nusselt number Nu. The Gunn (1978) correlation is employed, giving Nu as a function of the particle Reynolds number Re_p, the Prandtl number Pr, and the fluid volume fraction ε.

$$\begin{aligned} &\frac{dT_p}{dt} = \frac{S_p h}{m_p C_{p,p}}(\tilde{T} - T_p) + \dot{Q}_{ext} \\ &h = \frac{\lambda \mathrm{Nu}}{d_p} \end{aligned} \quad \Bigg| \quad \begin{aligned} \mathrm{Nu} = &\left(7 - 10\varepsilon + 5\varepsilon^2\right)\left(1 + 0.7\mathrm{Re}_p^{0.2}\mathrm{Pr}^{\frac{1}{3}}\right) \\ &+ \left(1.33 - 2.4\varepsilon + 1.2\varepsilon^2\right)\mathrm{Re}_p^{0.7}\mathrm{Pr}^{\frac{1}{3}}\,, \end{aligned} \tag{2.9}$$

where S_p and $C_{p,p}$ are respectively the particle surface and specific heat capacity.

The $\dot{Q}_{ext}$ term stands for the heat flux from external sources such as radiation, walls, or other particles. In this study, the bed temperature was maintained as a constant and, given that the thermal inertia of the particles is much larger than that of the gas, it is assumed that these external sources balance the exchanges with the gas phase and that the particle temperature is constant, i.e., $dT_p/dt = 0$. The coupling term in the gas phase enthalpy (Eq. 2.3) is written in order to ensure energy conservation as

$$\bar{\dot{Q}}_{p\to f} = -\frac{1}{\Delta V}\sum^{Np} S_p h(\tilde{T} - T_p)\,. \tag{2.10}$$

In the present work, the radiative heat transfer was neglected, as the total enthalpy budget analyzed by Hamidouche *et al.* (2016) reveals it to be negligible compared to heat transfer from combustion and hydrodynamics.

2.3. *Combustion modeling*

In this study, natural gas/air combustion is modeled using three kinetic schemes with Arrhenius reaction rates. The Dryer & Glassman (Dryer & Glassman 1973) and the BFER (Franzelli *et al.* 2012) schemes are two-step mechanisms with six transported species. The GRI 3.0 scheme (Smith *et al.* 1999) relies on 53 species and 325 reactions.

As the flame thickness of lean natural gas/air premixed flames is several orders of

magnitude smaller than the size of the FBR, combustion mainly occurs at the sub-grid scale. Moreover, the sub-grid scale closure must represent the different combustion regimes in the FBR: i) in the freeboard region, where a premixed flame propagates and ii) inside the bed, where combustion occurs in dense regions or in the void bubbles. The thickened flame for LES (TFLES) model (Colin *et al.* 2000) is considered here. In this model, diffusion of the species and temperature are artificially increased and the reaction source terms are decreased to thicken the flame front while keeping the correct propagation speed. It is particularly suited for the freeboard region. However, the model is not adapted in the dense regions, where the increase in the diffusivities may alter the heat exchanges with the particles and lead to unrealistic reaction zones. Therefore, a dynamic version of the TFLES model is preferred, in which the flame thickening is activated only where the flame freely propagates.

The TFLES model applied to the transport equation of species k reads

$$\frac{\partial}{\partial t}\left(\varepsilon\bar{\rho}\tilde{Y_k}\right) + \nabla.\left(\varepsilon\bar{\rho}\tilde{\mathbf{u}}\tilde{Y_k}\right) = \nabla.\left(\varepsilon\left[\bar{\rho}D_k\mathcal{E}\mathcal{F} + (1-\Omega)\frac{\mu_t}{Sc_t}\right]\nabla\tilde{Y_k}\right) + \frac{\mathcal{E}}{\mathcal{F}}\bar{\dot{\omega}}_k\,, \tag{2.11}$$

where $\mathcal{F}$, $\mathcal{E}$, Ω, D_k, μ_t, and Sc_t are respectively the thickening and efficiency functions, the flame sensor, the species diffusivity, the turbulent viscosity and the turbulent Schmidt number. μ_t is provided by the localized dynamic Smagorinsky model. The thickening factor is chosen constant in the flame front $\mathcal{F} = 1 + \Omega(\mathcal{F}_{max} - 1)$ and sufficiently large to ensure the minimal mesh resolution. $\bar{\dot{\omega}}_k$ is the k species source term.

The choice of the flame sensor Ω is very important as it has to ensure that mixing is altered only in the flame propagation zones. To this end, a progress variable is defined as $\tilde{c} = \widetilde{Y}_{CO} + \widetilde{Y}_{CO2}$ and its source term is $\bar{\dot{\omega}}_c = \bar{\dot{\omega}}_{CO} + \bar{\dot{\omega}}_{CO2}$. This source term has a maximum value in the propagation regions denoted as $\max(\bar{\dot{\omega}}_c)$. Then, the flame sensor is defined as follows: $\Omega = 1$ if $\bar{\dot{\omega}}_c$ exceeds 10% of $\max(\bar{\dot{\omega}}_c)$ locally or in the neighboring control volumes and $\Omega = 0$ elsewhere. The neighboring cell stencil is composed of two layers of control volumes connected to the local control volume. This definition ensures that the flame is properly thickened in the propagation regions and that mixing is not altered in the dense regions, where combustion is mitigated by heat transfer with the particles.

2.4. *Flow solver*

All the numerical simulations have been performed using the finite-volume code YALES2 (Moureau *et al.* 2011*a*), an LES/DNS solver based on unstructured meshes. This code solves the low-Mach number Navier-Stokes equations for turbulent reactive flows using a time-staggered projection method for variable density flows (Pierce & Moin 2004). YALES2 is specifically tailored to solve these low-Mach number equations on massively parallel machines on billion-cell meshes thanks to a highly optimized linear solver (Moureau *et al.* 2011*b*).

Recently, in the framework of the MORE4LESS project funded by the French National Research Agency and coordinated by IFP-EN, the DEM described in Section 2.1.2 for the modeling of solid particles has been implemented in the YALES2 solver. The DEM solver has been thoroughly optimized for massively parallel computing: it features a dynamic collision detection grid for unstructured meshes and packing/unpacking of the halo data for non-blocking MPI exchanges.

A critical point in this coupling is the time advancement of the gas and solid phase equations as they have very different time scales. The choice was made to sub-step the solid phase, whose time advancement is limited by the collision time step, during a gas phase time step, which is itself governed by convective and diffusive time scales.

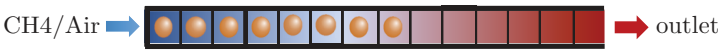

Figure 2: 1D static bed configuration

2.5. *Validation of the CFD/DEM solver*

The coupled CFD/DEM solver has been thoroughly validated on different benchmark cases: i) particle/particle and particle/wall collisions to assess the time step limits and the kinetic energy conservation, ii) 3D static beds to verify the close packing limit, iii) minimal fluidized beds to assess the minimum fluidization velocity, and iv) the freely-falling point particle case to estimate the drag force errors similarly to Horwitz & Mani (2016). In this latter case, a single freely-falling particle is placed randomly in a closed computational domain consisting of tetrahedra. Then, the error on the free-fall velocity due to the gas velocity field disturbance created by the particle is measured. With the parameters of the present study, i.e., particles that are twice as small as the cell size and $\mathrm{Re}_p = 60$, the maximum error on the free-fall velocity was 12%.

3. Results and analysis

In this section, three different test cases of increasing complexity are presented. They aim at evaluating the combustion modeling strategy and bringing insight into FBR combustion regimes.

3.1. *1D static bed*

The purpose of this first test case is to quantify the impact of the chemical mechanism on the FBR modeling approach. The test case is illustrated in Figure 2. It consists of a static bed with 80 fixed particles. The Eulerian grid features a single cell in the two periodic cross directions and 400 cells in the flow direction, whose size is equal to the particle size. The size of the cells in the cross directions is a variable parameter to achieve the desired fluid volume fraction. A lean mixture of air and methane is injected in the static bed at a fraction of the laminar flame speed $u_{in} = S_L/5$. The equivalence ratio is the same as the targeted FBR, i.e., $\phi = 0.83$. The flow is ignited by heating the particles above $1800K$. Then, particles are cooled down to the desired bed temperature. When a steady state is reached, two different situations are obtained: a premixed flame stabilizes above the bed or methane conversion occurs mainly inside the static bed. The two situations may be differentiated based on the location of the maximum of the methane conversion rate $|\dot{\omega}_{CH_4}|$. In this part, the $\mathcal{F}_{max}$ factor involved in Eq. (2.11) is set to 10.

The parametric study is presented in Figure 3 for the three considered mechanisms and for the two particle diameters used in this study. The reference case is the GRI3.0 case, as it provides the most detailed mechanism. First, it can be observed that the GRI3.0 and Dryer & Glassman mechanisms give a similar combustion regime distribution for the same particle size. Interestingly, the combustion regime transition curve crosses the experimental critical temperature line at fluid volume fraction greater than 0.9 for small particles, indicating that a flame may propagate only in the void regions for a bed temperature below the critical value. However, the BFER mechanism leads to a very different combustion regime map, where methane conversion may occur at low temperature and small fluid fraction. This is due to the fact that the BFER scheme was designed to give a correct flame speed for a range of equivalence ratios but not optimized for auto-ignition problems. The activation energy of the methane conversion reaction is smaller than that

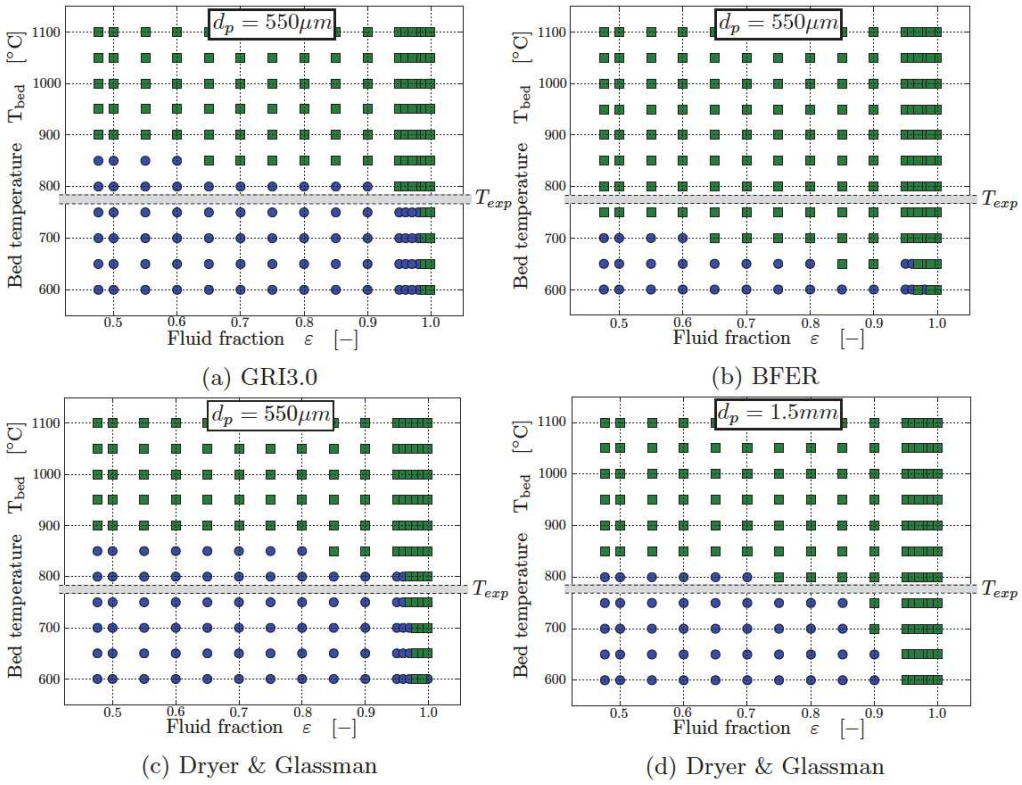

Figure 3: Combustion regime maps obtained with different kinetic schemes. The main reaction zone is located: ● above the bed or ■ inside the bed. T_{exp} is the critical bed temperature reported in Dounit *et al.* (2008)

.

of the Dryer & Glassman mechanism. Finally, the size of the particles has a non-negligible effect on the transition, especially in terms of fluid volume fraction. This influence may be explained by neglecting the transport and diffusion effects inside the static bed in the gas temperature equation

$$\frac{d\tilde{T}}{dt} = \frac{\dot{\omega}_T}{\bar{\rho} C_p} + \frac{1-\varepsilon}{\varepsilon} \frac{6 Nu\, D_{th}}{d_p^2} (T_p - \tilde{T}) \,, \tag{3.1}$$

where $\dot{\omega}_T$ and D_{th} are the reaction source term and the thermal diffusivity of the gas, respectively. The second term on the RHS is the heat transfer with the particles. All things being equal, the ratio $(1-\varepsilon)/(\varepsilon d_p^2)$, which is directly linked to the surface-to-volume ratio of the particles, is the driving term in the gas temperature evolution. It explains why combustion may occur at the same temperature in a bed with larger particles at smaller fluid fraction. The Dryer & Glassman mechanism is retained in the following work.

3.2. *Small-scale FBR*

The aim of this test case is to reproduce the dynamics and the combustion regime of the semi-industrial configuration at a smaller scale. The considered configuration is depicted in Figure 4. It consists of a cylinder meshed with 9 million tetrahedra, which contains

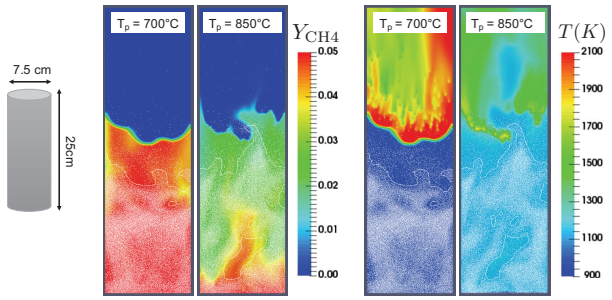

Figure 4: Small-scale FBR with d_p = 550 microns. Left: configuration. Middle: instantaneous CH_4 mass fraction in the mid-plane. Right: instantaneous temperature.

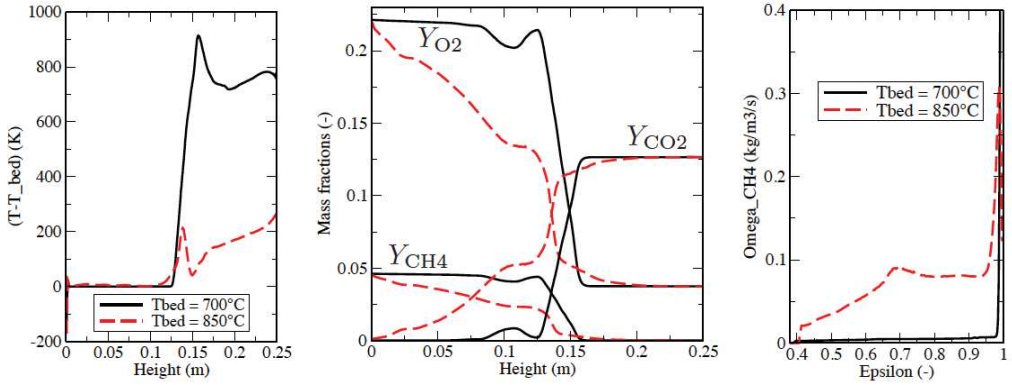

Figure 5: Statistics of the small-scale FBR: mean temperature difference at the centerline (left), mean species mass fractions at the centerline (center), mean species mass fractions at the centerline (right).

1.7 million particles of diameter d_p = 550 microns. The cell size is approximately 1 mm, i.e., twice as large as the particle diameter. In this part, the $\mathcal{F}_{max}$ factor involved in Eq. (2.11) is set to 10. A lean CH_4/air mixture at 300 K is injected at the bottom of the bed at twice the minimum fluidization velocity. This regime is referred to as the bubbling regime, in which void zones appear at the inlet and are convected by the bed's hydrodynamic towards the surface. Figure 4 also presents instantaneous CH_4 mass fraction and temperature in the mid-plane for two values of the particle temperature T_p. One of these values is above the critical bed temperature T_c and the other is below. The figure shows that below T_c, CH_4 is not converted in the bed and a premixed flame is lifted above the bed. With a higher bed temperature, CH_4 is converted inside the bed and temperature is homogenized, as observed in the experiment (see Figure 1).

These conclusions are confirmed by the temperature difference and species mass fraction statistics at the centerline of the FBR or by the CH_4 source term conditioned by the fluid volume fraction in Figure 5. As in the experiment, at high bed temperature, the temperature jump between the bed and the freeboard region is small. In this case, methane conversion occurs in the bed, and combustion is almost complete when the flow enters the freeboard region. The lower temperature case brings a different picture: a strong jump is observed for all the profiles, revealing the presence of a premixed flame.

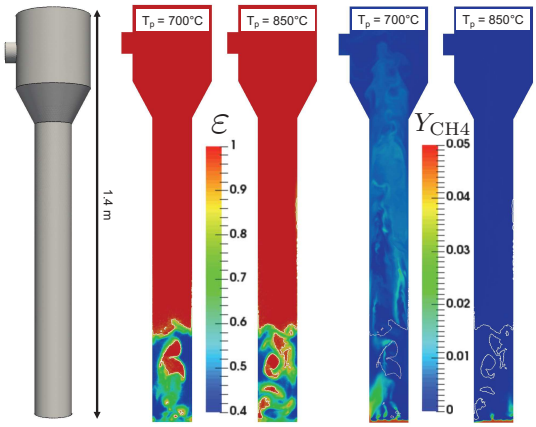

Figure 6: Semi-industrial FBR with d_p = 1.5 mm. Left: configuration; middle: instantaneous fluid fraction; right: instantaneous CH_4 mass fraction. White iso-line: $\varepsilon = 0.9$.

It should be noted that not all of these profiles can be directly compared to the experiment due to the different size of the bed and of the particles (550 microns in the small-scale FBR versus 350 microns in the experimental case of Figure 1), the constant particle temperature hypothesis and the omission of radiative heat transfer in the burnt gases, which makes the temperature decrease in the freeboard region.

3.3. *Application to the semi-industrial FBR*

The experimental FBR presented in Figure 1 has a 1400-mm-high cylindrical shape with a diameter of 180 mm, where temperature, pressure drop, and major species mole fractions are measured. This cylinder is topped with a disengaging section where the burnt-gases exhaust is located. The FBR is fed at the bottom with a mixture of natural gas and air with an excess air factor ranging from 1.0 to 1.5. Only the excess air factor of 1.2 is considered here. The FBR contains 12 kg of sand particles with a density of 2650 kg.m^{-3}. Three different particle diameters have been investigated experimentally: 100, 350, and 550 microns. The flow velocity at the inlet is chosen to be twice the minimum fluidization velocity to achieve a bubbling regime.

In the experimental reference case, the mean particle diameter is 350 microns. With these properties, approximately 200 million particles are present in the FBR. Before performing such large-scale simulations, a first step is taken with a particle diameter of 1.5 mm, resulting in approximately 2.6 million particles. This diameter value is significantly larger than the experimental values, which has a strong impact on methane conversion (Dounit *et al.* 2008). The Eulerian mesh counts 33 million tetrahedra with a homogeneous size of 2 mm in the dense region. $\mathcal{F}_{max}$ factor from Eq. (2.11) is set to 60.

Preliminary results are presented in Figure 6. This figure illustrates the strong dynamics obtained in the bed and the impact of the particle temperature on CH_4 conversion. In the hot case, CH_4 is rapidly converted, whereas it is still present in the cooler case. From the analysis in Section 3.1, this difference is likely to be more pronounced with smaller particles as the heat exchanges between the two phases will be significantly augmented.

Acknowledgments

This work was partially supported the French National Research Agency (ANR) as part of the "Energy efficiency of processes and systems" Program (ANR-14-CE05-0042).

REFERENCES

Capecelatro, J. & Desjardins, O. 2013 An Euler-Lagrange strategy for simulating particle-laden flows. *J Comput. Phys.* **238**, 1–31.

Colin, O., Ducros, F., Veynante, D. & Poinsot, T. 2000 A thickened flame model for large eddy simulations of turbulent premixed combustion. *Phys. Fluids* **12**, 1843–1863.

Cundall, P. A. & Strack, O. D. L. 1979 A discrete numerical model for granular assemblies. *Geotechnique* **29**, 47–65.

Dounit, S., Hemati, M. & Andreux, R. 2008 Modelling and experimental validation of a fluidized-bed reactor freeboard region: Application to natural gas combustion. *Chem. Eng. J.* **140**, 457–465.

Dounit, S., Hemati, M. & Steinmetz, D. 2001 Natural gas combustion in fluidised bed reactors between 600 and 850°c: experimental study and modelling of the freeboard. *Powder Technol.* **120**, 49–54.

Dryer, F. L. & Glassman, I. 1973 High-temperature oxidation of CO and CH4. *Symposium (International) on Combustion* **14**, 987–1003.

Ergun, S. 1952 Fluid flow through packed columns. *Chem. Eng. Prog.* **48**, 89–94.

Esteghamatian, A., Bernard, M., Wachs, A., Lance, M. & Hammouti, A. 2015 Micro/meso simulations for fluidized beds. In *Proc. of CHT-15. 6th Int. Symposium on Advances in Computational Heat Transfer*.

Franzelli, B. G., Riber, E., Gicquel, L. & Poinsot, T. 2012 Large eddy simulation of combustion instabilities in a lean partially premixed swirled flame. *Combust. Flame* **159**, 621–637.

Gunn, D. J. 1978 Transfer of heat or mass to particles in fixed and fluidised beds. *Int. J. Heat Mass Tran.* **21**, 467–476.

Hamidouche, Z., Masi, E., Fede, P., Simonin, O., Ansart, R., Dounit, S. & Hemati, M. 2015 3D numerical simulation of natural gas combustion in a fluidized bed reactor. In *22nd Int. Conf. on Fluidized Bed Combustion*.

Hamidouche, Z., Masi, E., Fede, P., Simonin, O., Ansart, R. & Hemati, M. 2016 Unsteady three-dimensional numerical simulations of methane combustion in dense fluidized bed. In *9th Int. Conf. on Multiphase Flow*.

Horwitz, J. & Mani, A. 2016 Accurate calculation of Stokes drag for point–particle tracking in two-way coupled flows. *J Comput. Phys.* **318**, 85–109.

Moureau, V., Domingo, P. & Vervisch, L. 2011*a* Design of a massively parallel CFD code for complex geometries. *CR Mécanique* **339**, 141–148.

Moureau, V., Domingo, P. & Vervisch, L. 2011*b* From large-eddy simulation to direct numerical simulation of a lean premixed swirl flame: Filtered laminar flame-pdf modelling. *Combust. Flame* **158**, 1340–1357.

Pierce, C. D. & Moin, P. 2004 Progress-variable approach for large-eddy simulation of non-premixed turbulent combustion. *J. Fluid Mech.* **504**, 73–97.

Smith, G. P., Golden, D. M., Frenklach, M., Moriarty, N. W., Eiteneer, B., Golden-berg, M., Bowman, T. C., Hanson, R. K., Song, S., Jr, W. C. G. & et al 1999 Gri-Mech 3.0.

Wen, C.-Y. & Yu, Y. H. 1966 A generalized method for predicting the minimum fluidization velocity. *Amer. Inst. Chem. Eng. J.* **12**, 610–612.